ATMOSPHERIC SCIENCE

Atmospheric rivers over eastern US affected by Pacific/North America pattern

Wenhao Dong[1,2]*, Ming Zhao[2], Zhihong Tan[3], V. Ramaswamy[2]

Atmospheric rivers (ARs) play important roles in various extreme weather events across the US. While AR features in western US have been extensively studied, there remains limited understanding of their variability in the eastern US (EUS). Using both observations and a state-of-the-art climate model, we find a significant increase (~10% dec^{-1}) in winter AR frequency in the EUS during the past four decades. This trend is closely linked to recent changes in the Pacific/North America (PNA) teleconnection pattern, accompanied by a poleward shift of the mid-latitude jet stream. We further reveal a strong correlation ($R = 0.8$; $P < 0.001$) between interannual variations in AR occurrence and the PNA index. This linkage has been verified in various model simulations. A statistical model, built on this linkage, has proven effective in predicting the AR frequency using the PNA index at both monthly and seasonal scales. These promising results have important implications for addressing concerns related to AR-associated extreme precipitation and flooding in this region.

INTRODUCTION

Atmospheric rivers (ARs) are synoptic-scale weather features characterized by long, narrow flows of moist air that can transport enormous amounts of water vapor poleward. ARs play a vital role in the global hydrological cycle, responsible for roughly 90% of the poleward moisture transport in the mid-latitudes (*1*–*7*). Winter ARs are of particular importance to the US West Coast as they are very effective at producing impactful precipitation when they impinge on the mountains (*2*, *8*). While they act as the drought buster along the US West Coast: 33 to 74% of the persistent droughts from 1950 to 2010 were ended by the arrival of landfalling AR storms (*9*), they are also the primary drivers of flood damages there: ARs generated most of the observed high daily runoff in the western US (WUS) during water years 1949–2015 (*10*–*12*).

ARs in the eastern US (EUS) remains relatively understudied, despite their frequent occurrence and substantial contribution to the heavy precipitation and high-impact weather events (*13*–*15*). Approximately 30 to 35% of annual precipitation over a broad area of EUS can be attributed to AR activity, and ARs are responsible for over 60% extreme precipitation events and more than 70% flood events across the EUS (*16*, *17*). In addition, year-to-year variations in total precipitation can be largely explained by changes in AR-related precipitation (*18*–*20*). A couple of studies have examined the trend in AR intensity [measured by the magnitude of integrated vapor transport (IVT)] and size over the EUS (*16*, *21*). However, the trend in AR frequency and the driving factors in winter, when ARs have largest impacts on extreme rainfall, remains unclear, raising substantial concerns regarding flooding in densely populated areas (*16*, *22*).

In this study, we conduct a comprehensive analysis of the variability and trend of winter (December-January-February) AR frequency in the EUS over the past four decades, as winter exhibits the highest AR frequency and they exert a greater impact on the winter mean and extreme precipitation (*16*). To identify the potential driving factors, we examine the links between AR variability and multiple climate variability modes. These correlations are examined using a set of simulations with a high-resolution climate model developed at the Geophysical Fluid Dynamics Laboratory (GFDL), which has the capability to explicitly simulate ARs. Our results reveal that recent shift in the Pacific/North America (PNA) teleconnection pattern from positive to negative phase is closely associated with a poleward shift of the mid-latitude jet stream, which favors an increase in AR frequency in the EUS. The PNA index has proven effective in predicting and understanding the AR frequency at both monthly and seasonal timescales. With the PNA index's notable predictability over 1 to 2 months (*23*, *24*), this relationship suggests the potential for enhancing AR frequency predictions in the EUS.

RESULTS

AR features in the EUS

Figure 1A shows a category 5 AR event (*6*) that occurred over the EUS from 8 to 11 February 2013. It formed over Texas and propagated from the western part of Southeast to the upper Midwest, reaching its peak IVT of more than 1000 kg m^{-1} s^{-1} by 10 February. This AR event produced record precipitation (>50 mm day^{-1}) centered around Alabama (Fig. 1, B and C). Remarkably, this event ranked the second largest February rainfall in the 50-year record for Alabama. While it provided the much-needed relief from the region's two-and-a-half-year drought, it triggered multiple flash floods and landslides. Additionally, this storm brought hails, wind gusts, and 10 tornados (including 1 EF-4 tornado) along its path, causing widespread damage and resulting in losses exceeding $39 million (*25*).

On average, the AR frequency during the winter season in the EUS is about 10%, which is comparable to the frequency in the WUS (Fig. 1D). The North Pacific and North Atlantic Oceans exhibit peak winter AR frequency rates exceeding 12% (Fig. 1D). These high frequencies extend from coastal area inland, making the Pacific Northwest and Southeast notable with more AR events. The ARs contribute to 25% to 55% of the total precipitation over the EUS (*13*, *26*), which is similar to the contribution of approximately 40% across the WUS (*17*, *27*–*31*) (Fig. 1E). Note that the percent values of related precipitation are slightly smaller than some existing analyses based on daily datasets (*4*, *30*). This is due to the use of a 6-hour dataset in our analysis, which only accumulates

[1]Cooperative Programs for the Advancement of Earth System Science, University Corporation for Atmospheric Research, Boulder, CO, USA. [2]NOAA/Geophysical Fluid Dynamics Laboratory, Princeton, NJ, USA. [3]Program in Atmospheric and Oceanic Sciences, Princeton University, Princeton, NJ, USA.
*Corresponding author. Email: wenhao.dong@noaa.gov

precipitation totals during 6-hour increments of AR activity. This conservative approach may have important implications to flash floods.

Increasing AR frequency

Large and significant ($P < 0.05$) increases in winter ARs are observed over the EUS during 1980–2020 (Fig. 2A). The Southeast region exhibits the largest increases, with a rate of 0.1 fraction of time per decade (or equivalently 10% per decade). The maximum axis of these increases is located on the poleward flank of the long-term mean, indicating a poleward shift of AR activity. This shift could substantially affect AR-associated precipitation patterns. Both the long-term mean and linear trend are remarkably similar when we use the MERRA2 dataset (fig. S1), and the findings are consistent with those reported before using different methods and

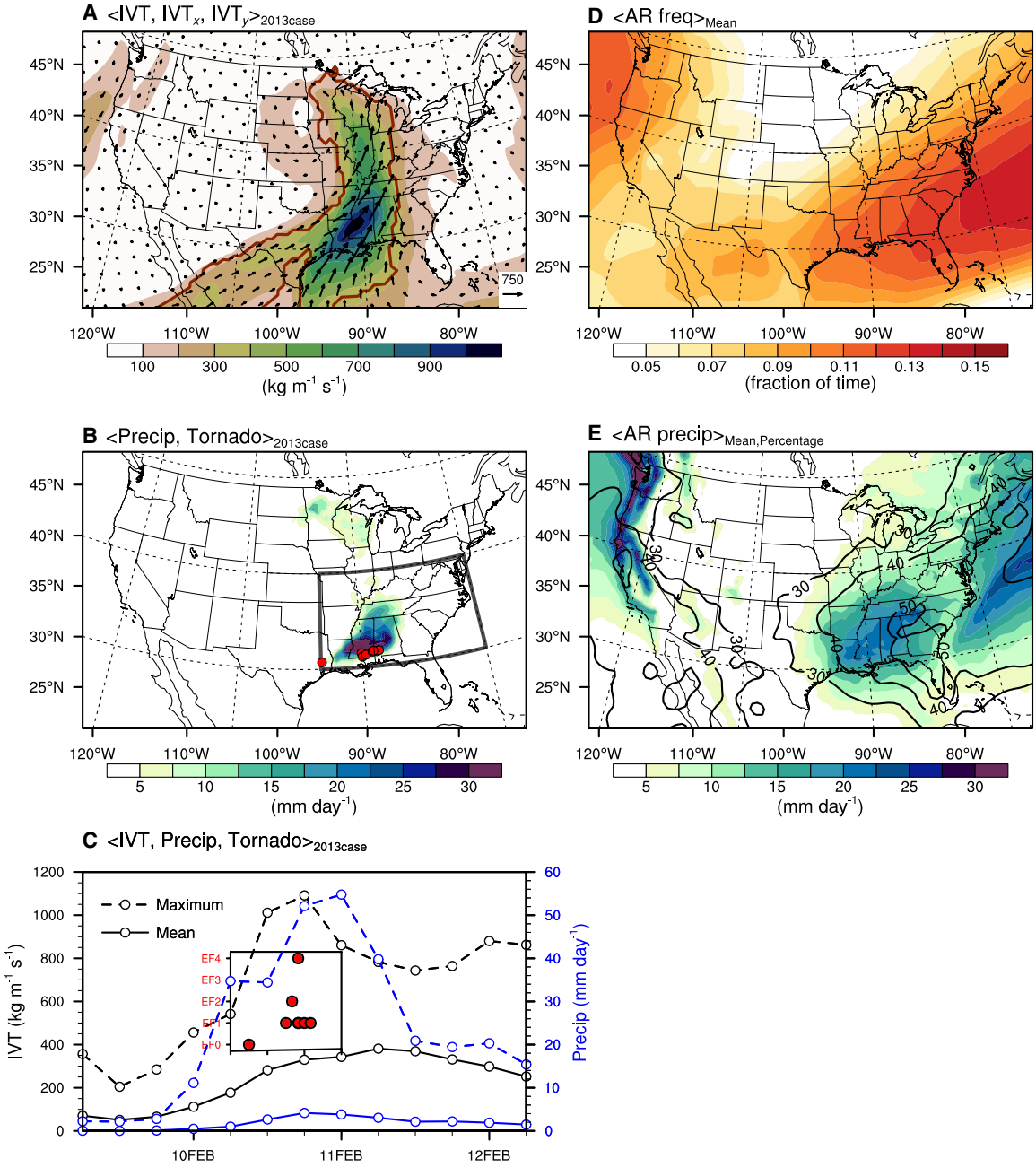

Fig. 1. Atmospheric river features in the eastern US. (**A** and **B**) Integrated vapor transport [IVT (A)] and precipitation (B) for one atmospheric river (AR) event on 10 February 2013 based on the Fifth Generation of the European Centre for Medium-Range Weather Forecasts (ECMWF) Reanalysis (ERA5) and the Multi-Source Weighted-Ensemble Precipitation (MSWEP) datasets. Red dots in (B) denote the tornados that occurred during 9 to 12 February 2013. (**C**) Time series of the domain average [black rectangle in (B)] IVT (black) and precipitation (blue) for the AR event during 9 to 12 February 2013. Solid (dashed) lines represent the mean (maximum) values. The inset plot shows the scale (*y* axis) and timing (*x* axis) of the tornados. (**D** and **E**) Winter mean AR frequency (D) and AR-associated precipitation (E) during the period of 1980–2020. Contour in (E) denotes the percentage of AR-associated precipitation to total winter mean precipitation.

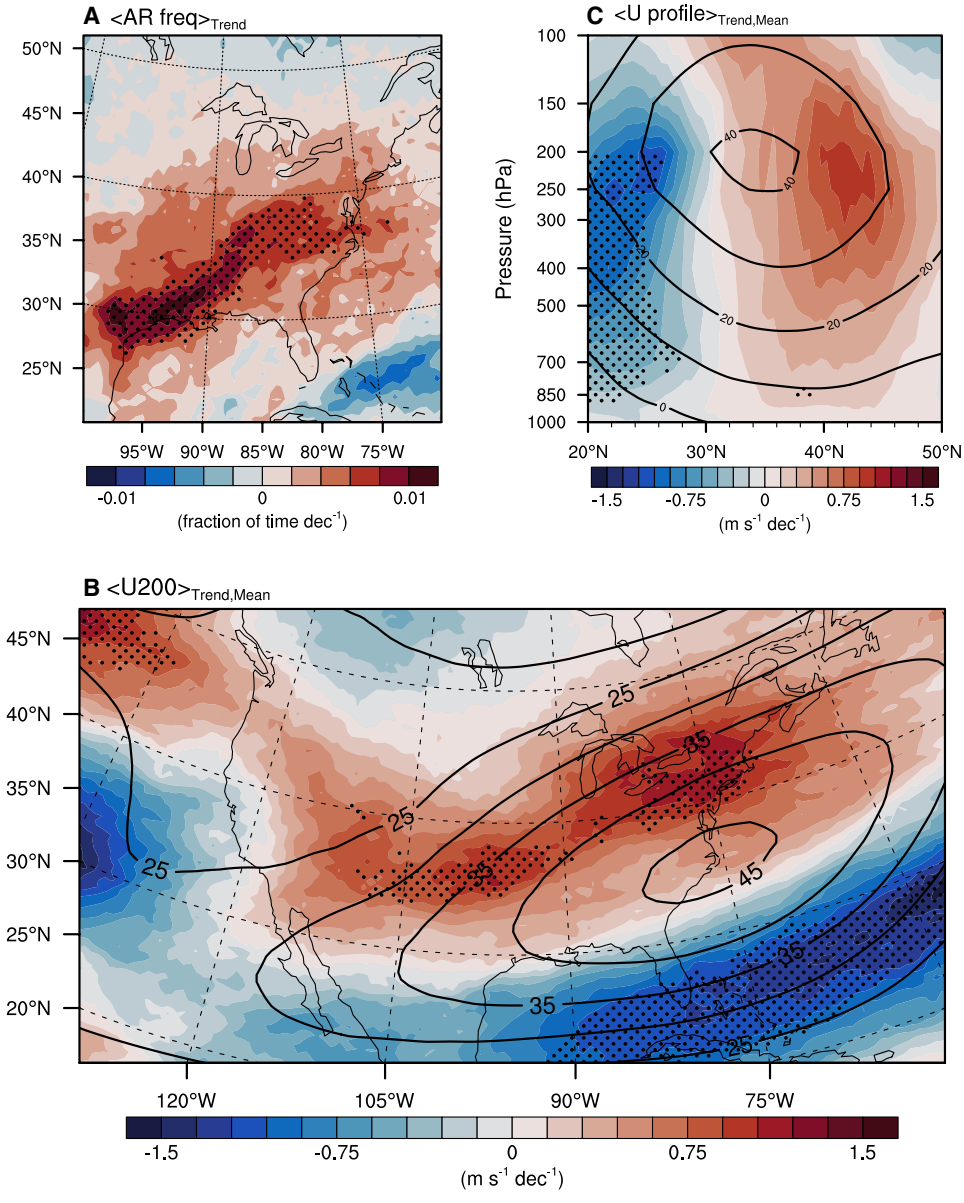

Fig. 2. Changes in atmospheric river frequency and the mid-latitude jet. (**A** to **C**) Linear trend of winter atmospheric river (AR) frequency (A), zonal wind at 200 hPa (B), and zonal wind vertical profile averaged over 95°W to 75°W (C) during 1980–2020 based on the ERA5 dataset. Contours in (B) and (C) represent the respective mean of the zonal wind during the same period. Stippling in (A) to (C) denotes regions with trends significant at the 95% confidence level.

datasets (*4*, *30*–*32*). This agreement reinforces the robustness of our analysis and conclusions.

ARs are commonly regarded as integral components of extratropical cyclones, influenced by the steering flow and associated jet streams, which include both eddy-driven and subtropical components (*7*). In the mid-latitudes, the dominant zonal wind component often serves as a proxy for the steering flow (*33*). When regressed against the zonal wind, AR frequency is found to be positively correlated with the upper troposphere wind within the 30°N to 50°N latitude band over the EUS, while negative correlations are evident for latitudes south of 30°N (fig. S2). These patterns are also discernible and located slightly southward in the lower troposphere, where most of the moisture transport occurs. The vertically poleward-tilted relationship between zonal wind and AR frequency is indicative of baroclinicity, which will be further examined later. Analysis of zonal wind confirms that the upward trend in AR frequency is associated with a strengthening and poleward shift of the mid-latitude jet stream over North America (Fig. 2, B and C). The northward shift has been previously reported and linked to changes in winter mid-latitude weather systems (*34*, *35*). The resultant southwest-to-northeast aligned steering flow favors more stronger storms propagating toward the EUS.

The role of the mid-latitude jet stream in AR activity is mirrored in changes in baroclinic instability, which is the predominant driver of mid-latitude winter storms (*36*–*38*). As measured by the maximum Eady growth rate (EGR), strong baroclinicity is distributed over broad regions of the EUS and the adjacent ocean, suggesting favorable

conditions for storm generation and/or development (fig. S3). The observed increase in AR frequency is consistent with changes in EGR, characterized by large positive trends over the EUS. This increase is dynamically linked to enhanced vertical wind shear (Fig. 2C), an important contributor to the EGR, supporting the observed intensification and poleward shift of ARs. Similar patterns of jet streams, EGR, and their changes are also found in the MERRA2 dataset (fig. S4).

Link to the PNA pattern

Previous correlation analysis has revealed that many climate modes, including El Niño/Southern Oscillation (ENSO), PNA pattern, Pacific-Japan (PJ) teleconnection pattern, East Asia subtropical jet (EASJ), and others, are important drivers of AR activity, primarily observed over the WUS (*4*, *16*, *39*–*42*). We replicate the correlation analysis to investigate which climate mode is most relevant to the observed increase in AR frequency over the EUS.

Figure 3A and fig. S5 show the interannual variations of different climate modes and AR frequency over the EUS (averaged over 30°N to 40°N, 95°W to 75°W). The PNA index presents the highest correlation coefficient ($R = -0.80$; $P < 0.001$) with AR frequency (Fig. 3A and figs. S5 and S6). The spatial distribution of the observed AR trends is also clearly revealed in the point-wise correlation maps between the PNA index and AR frequency (Fig. 3C and fig. S7). While the spatial patterns for PNA, PJ, and EASJ are similar due to their intrinsic connection with the Asian-Pacific jet (figs. S5 and S6), the correlation coefficients between the PNA index and AR frequency are much higher and their spatial distributions are more coherent. This can be attributed to the distinct nature of the PNA pattern, which often features an amplified ridge-trough configuration within the jet stream over North America. Such a pattern tends to last over extended periods, exerting a notable influence on the trajectories of storms and weather systems as they traverse the EUS. Furthermore, the time series of AR frequency is correlated with the 500-hPa geopotential height field, which well reproduces the classical negative phase of the PNA pattern (Fig. 3D), highlighting the intimate relationship between the PNA pattern and AR frequency over the EUS. When we replace seasonal means with monthly values, the correlation coefficient decreases largely for all climate modes (figs. S8 and S9) but remains high ($R = -0.67$; $P < 0.001$) for the PNA index. These results suggest that the recent trend in PNA pattern is important for the observed increase in AR frequency over the EUS.

The transition from a positive phase of PNA to a negative phase has substantial impacts on large-scale circulation patterns. Correlating the PNA index with the zonal winds and EGR reveals similar patterns to the respective linear trends (Fig. 3, B and C, and fig. S3). This suggests that the observed variation in the jet stream and baroclinic instability is largely related to recent changes in the PNA pattern. Our results support previous findings that there is a poleward shift of the mid-latitude jet over North America in the negative phase of the PNA pattern (*43*). These changes favor the northward propagation of warm and moist air from the Gulf of Mexico and the Atlantic, resulting in more ARs affecting the EUS. Consistent results are obtained in the composite analysis based on different PNA phases (fig. S10). These consistencies, in conjunction with the correlation analysis, highlight the importance of the PNA pattern in affecting AR activity over the EUS.

Verification in climate model simulation and prediction

To further study the robustness of the relationship between PNA pattern and AR frequency over the EUS, and whether the observed relationship is due to other modes of variability, particularly ENSO given its influence on the PNA pattern (see fig. S6 for their interrelationships), we perform a 10-member ensemble Atmospheric Model Intercomparison Project. (AMIP)-type simulation using the high-resolution (~50-km) GFDL AM4 model. The individual realizations of the multi-member ensemble allow for a diversified evolution of the PNA pattern under the same time evolution of ENSO condition and other forcing conditions [i.e., through prescribed sea surface temperatures (SSTs), sea ice, radiative gases, and aerosols]. Considering that the PNA pattern is a natural internal mode of climate variability, the model spread can be solely attributed to the atmospheric internal variability (as detailed in Materials and Methods).

Consistent with previous studies (*30*, *31*), the mean AR frequency is well simulated; however, the linear trend diverges dramatically among the ensemble members (fig. S11). In addition, the temporal correlation coefficients between the simulated AR frequencies and the observed ones vary widely across the ensemble members at both seasonal (0.07 to 0.42) and monthly (0.01 to 0.30) timescales (Fig. 4A and fig. S12). This indicates that the variability of winter AR activity is not determined to the first order by the prescribed SST and sea-ice conditions, but instead arises from internal variability. Similarly, the simulated time series of PNA patterns also exhibit substantial variation among the ensemble members (Fig. 4A and fig. S13), with the model-observation correlation coefficient ranging from 0.29 to 0.68 (the ensemble mean of 0.63) at seasonal timescale. The values are smaller at monthly timescale.

Despite large variations in the simulated time series of AR frequency and PNA index, there is a consistent relationship between the two. In general, the members that exhibit a better simulation of the PNA pattern also demonstrate a more accurate representation of the observed AR frequency variability ($R = 0.82$, $P < 0.001$; Fig. 4A). Moreover, when we repeat the correlation analysis between the PNA index and the AR frequency, the observed relationship is well reproduced in all ensemble members at both timescales, with the ensemble mean correlation coefficients of about 0.8 and 0.6, respectively (Fig. 4B and fig. S14). The robustness of this relationship across a variety of time evolution of the PNA index substantiates its important linkage with AR activity over the EUS. This relationship is also consistent with a nudged simulation, in which model horizontal winds are nudged toward reanalysis data with the model's thermodynamical variables such as temperature and humidity freely evolving and generating variations of clouds and precipitation (see Materials and Methods). Compared to the other 10 simulations, the nudged experiment well captures the spatial distribution of AR frequency as well as its increasing trend over the EUS, albeit the trends are slightly weaker (figs. S11 to S14). This indicates that when the model's circulation, including the PNA pattern, is constrained by the observations, the model can very well reproduce both observed AR frequency variability and trend over the EUS.

This strong relationship between PNA pattern and EUS AR variability has important implications for the subseasonal to seasonal prediction of AR frequency. We assess the predictability of AR frequency in the EUS with a statistical model by conditioning it on the PNA pattern and validate the predictions using a leave-one-out criterion (see Materials and Methods). The results demonstrate that this statistical model effectively captures the year-to-year variability in AR frequency ($R = 0.78$, $P < 0.001$; Fig. 3B), with both the root mean squared error (RMSE) and mean absolute error (MAE) close to 1. The predictability at the monthly scale has also been evaluated with a correlation efficiency of 0.62 ($P < 0.001$) (fig. S15). This result

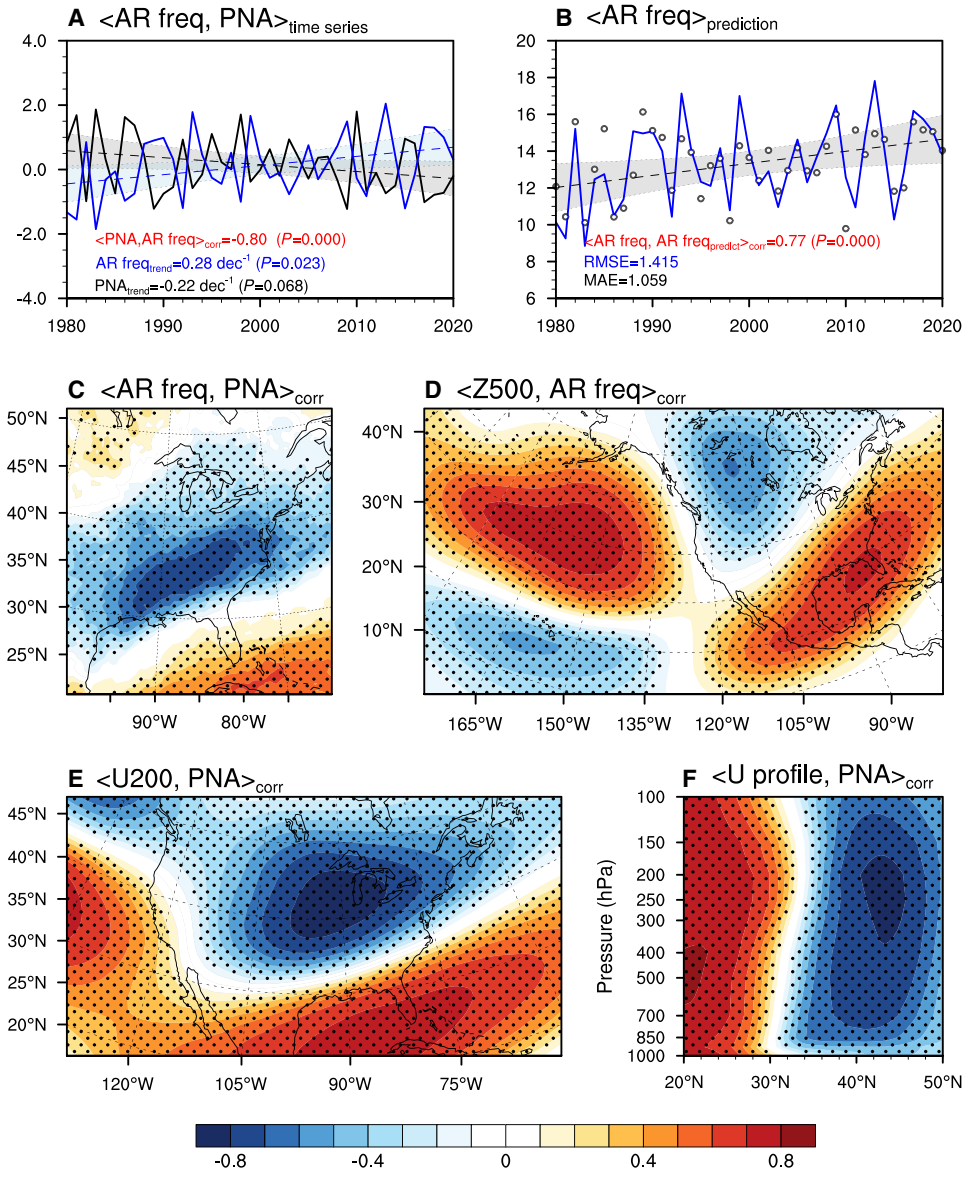

Fig. 3. Linkage between atmospheric river frequency and the Pacific/North American pattern. (**A**) Time series of winter Pacific/North American (PNA) index (black) and the normalized winter atmospheric river (AR) frequency (blue; averaged over 30°N to 40°N, 95°W to 75°W) based on the ERA5 dataset during the period of 1980–2020. The best linear fit and prediction errors are represented by the dashed line and shading, respectively. Linear trends for PNA index and AR frequency, as well as their correlation, are listed. (**B**) Time series of winter AR frequency (blue line) and the predicted winter AR frequency (black circle) during the period of 1980–2020. The root mean squared error (RMSE), mean absolute error (MAE), and correlation coefficient are listed. (**C**) Correlation map between winter PNA index and winter AR frequency. (**D**) Correlation between the eastern US winter AR frequency and geopotential height at 500 hPa using ERA5 dataset. (**E** and **F**) Correlation between winter PNA index and zonal wind at 200 hPa (E), and zonal wind profile averaged over 95°W to 75°W (F). Stippling in (B) to (F) denotes regions with correlation coefficient significant at the 95% confidence level.

will be valuable for better understanding and predicting AR-related high-impact weather events.

DISCUSSION

Using multiple observational datasets, we find that there is a significant increase in AR frequency over the EUS during the past four decades. This trend is mainly driven by changes in large-scale circulations, particularly the poleward shift and strengthening of the mid-latitude jet stream over North America. The PNA pattern has been found to play a critical role in this transition. As the PNA pattern shifts toward a more negative phase, it favors the northward transport of warm and moist air from the Gulf of Mexico and the Atlantic, associated with more ARs affecting the EUS. The correlation and composite analyses support the linkage between the PNA pattern and AR frequency. Our study revealed that the PNA pattern has a stronger influence on AR variability over the EUS than other climate modes, including Atlantic meridional mode (AMM), Arctic

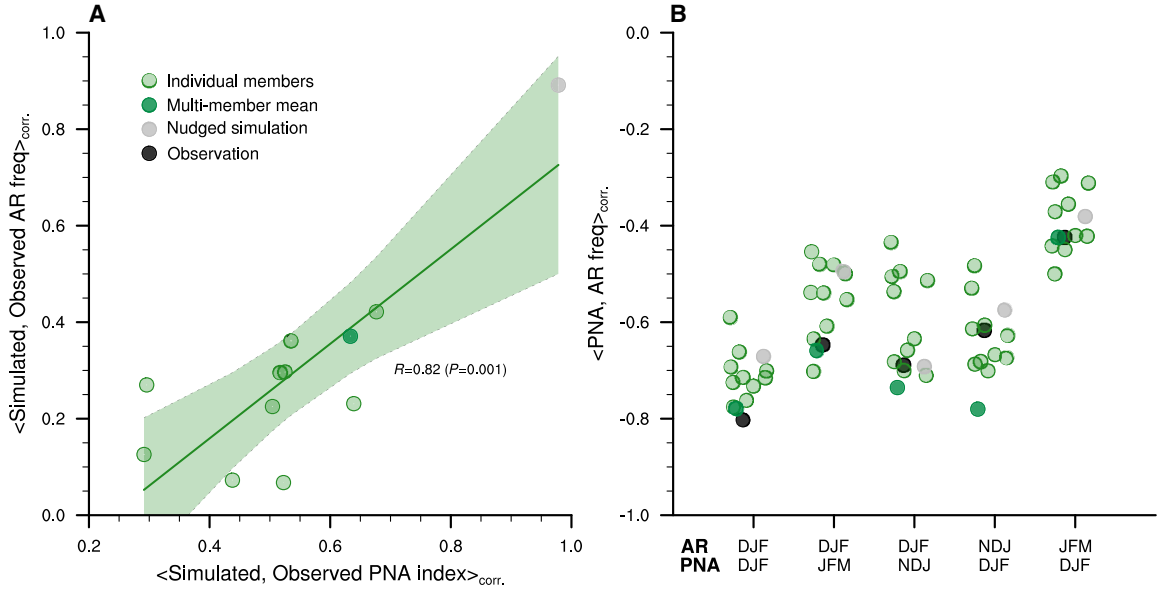

Fig. 4. Simulated atmospheric river frequency and the PNA index. (**A**) Scatterplot of correlation coefficients between the observed and simulated winter PNA index and the observed and simulated atmospheric river (AR) frequency averaged over 30°N to 40°N, 95°W to 75°W (as denoted by the black rectangle in Fig. 1B). The best linear fit and prediction errors are represented by the dashed line and shading, respectively. (**B**) Distribution of the lead-lag correlation coefficients between different seasonal PNA index and AR frequency averaged over 30°N to 40°N, 95°W to 75°W. Black circles represent the observational dataset, while green and gray circles are from the 10 ensemble members and the nudged simulation, respectively. The circles are randomly shifted horizontally for better illustration.

Oscillation (AO), EASJ, ENSO, North Atlantic Oscillation (NAO), Pacific Decadal Oscillation (PDO), Pacific meridional mode (PMM), and PJ, at both seasonal and monthly timescales.

A 10-member ensemble AMIP simulations using a high-resolution climate model confirmed the robustness of the AR frequency–PNA relationship, although it cannot reproduce the observed trend in AR frequency and PNA index, indicating that prescribed SST and sea-ice conditions alone would be insufficient to reproduce the historical AR trend in EUS. However, a nudged run that further constrains the atmospheric circulation can well reproduce the observed AR trend, indicating the crucial role of atmospheric circulation including the PNA pattern in affecting AR frequency variability and change over the EUS. A lead-lag correlation analysis has shown that the PNA index, even with a 1-month lead time, maintains a notable correlation with the AR frequency (Fig. 4B). But caution is needed as no statistically significant differences were found and the results displayed inconsistency when examining other seasons. This variability could be attributed to the inherent chaotic nature of the PNA pattern or suggest potential influence from other common drivers. The observed similarities in patterns between AR frequency over the EUS and various climate modes also imply that diverse atmospheric and oceanic variability, operating on diverse timescales, could result in varied impacts on AR frequency. Further investigation that incorporates a diverse set of other climate models would be useful to gain a comprehensive understanding of the intricate interactions involved. Nevertheless, the strong relationship would be useful for improved understanding and prediction of the winter AR over the EUS at both monthly and seasonal scales. With the promising prediction skill of the PNA index at lead time of 1 to 2 months during winter, it may provide some potential for subseasonal to seasonal forecasting of AR activity over the EUS, which could empower decision-makers to proactively prepare for potential AR-associated impacts, developing effective strategies to manage water resources and mitigate the effects of extreme weather events. It is worth noting that although this study examines the climate variability modes individually, they can evolve simultaneously in nature to alter regional conditions by complex interactions among atmospheric, land, and oceanic processes. Therefore, future efforts are needed to understand the existence and possible mechanism of combined impacts of these climate variabilities on AR activities over the EUS.

MATERIALS AND METHODS

Observational datasets

We use two reanalysis products to study AR features: The fifth generation European Centre for Medium-Range Weather Forecasts (ECMWF) reanalysis (ERA5) (*44*) at the resolution of 0.25° × 0.25° for the period of 1979–2020 and the National Aeronautics and Space Administration (NASA) Modern-Era Retrospective Analysis for Research and Application, version 2 (MERRA2) (*45*) at the resolution of 0.5° × 0.625° covering 1980–2020. ERA5 is improved with respect to its predecessor ERA-Interim (ERA-I) in simulating atmospheric dynamics. The latter is a widely used product for AR studies previously (*4*, *30*, *31*). MERRA2 is the default reference dataset for the AR Tracking Method Intercomparison Project (ARTMIP) (*5*, *46*). Both products have been used previously in the study of ARs, and results based on them are remarkably similar to other reanalysis products and/or different AR detection algorithms (*4*, *27*, *39*, *47*, *48*). In this study, the results based on ERA5 are presented in the main text, while those based on MERRA2 are available in the Supplementary Materials. The identification of ARs is based on the zonal and meridional column integrated water vapor transport (IVT), which are usually calculated using specific humidity and horizontal wind fields at multiple vertical levels. In this study, the internally derived zonal and meridional IVT in the reanalysis are used, which have the advantage of being calculated across internal model time steps

and on all the raw model vertical coordinates, not just over the interpolated standard pressure levels, and therefore may be preferable over coastal and mountainous regions. Other variables, including sea-level pressure, geopotential height, wind fields, temperature, and specific humidity from these two reanalysis products, are also used. The Multi-Source Weighted-Ensemble Precipitation, version 2 (MSWEP V2) (*49*) gridded precipitation dataset (0.1° × 0.1°) covering 1979–2020 is used as the main precipitation observation to explore the AR-related precipitation features. This product has been used to study the AR associated mean and extreme precipitation features (*31*).

Climate model simulations

We also analyze the simulated AR characteristics based on a high-resolution (~50-km) version of GFDL's atmospheric model AM4 (*50*, *51*). This model (referred to as C192AM4) (*28*) was used for GFDL's participation in the Coupled Model Intercomparison Project Phase 6 (CMIP6) HighResMIP project (*52*). It was also the atmospheric component of the GFDL's latest seasonal-to-decadal prediction system [the Seamless System for Prediction and EArth System Research (SPEAR)] (*53*), which has been previously used for AR prediction (*42*) and projection (*54*). The simulated IVT is also calculated across internal model time steps and on all the raw model vertical coordinates. We perform a 10-member ensemble simulation using the C192AM4 model, covering the period of 1980–2020, which is driven by the same observed SST and sea-ice conditions, greenhouse gases, and natural and anthropogenic aerosol emissions. The 10 members are generated by slightly perturbing the model's initial atmospheric conditions. Outputs from these simulations have been used to evaluate several important weather phenomena, such as ARs, tropical cyclones, and mesoscale convective systems (*30*, *31*, *55*, *56*), and the results have shown that this model is capable of simulating these systems reasonably well.

Considering that the PNA pattern constitutes a natural internal mode of climate variability, the ensemble configuration allows for diverse evolutions of the PNA pattern under identical ENSO conditions. The ensemble's multi-member mean serves as a means to assess the model's capability to replicate observed climate variability resulting from the prescribed external forcing, including SST and sea-ice conditions. Meanwhile, the spread among the multiple-member means serves as an indicator of uncertainties primarily stemming from atmospheric internal variability. Therefore, the impact of ENSO on the simulated AR variability can be assessed from the multi-member mean, while the impact of the PNA pattern on the simulated AR variability can be assessed from the spread of these members. Consequently, the impact of ENSO on the simulated variability of AR can be assessed by analyzing the multi-member mean, while the influence of the PNA pattern on the simulated AR variability can be evaluated by examining the variability among ensemble members.

In addition to these 10-member simulations, we conduct a nudged simulation in which the model's large-scale horizontal winds are nudged to align with reanalysis data. Other variables, including temperature, humidity, clouds, and precipitation, are computed interactively within the model, subject to the same dynamic and physical processes as in the other simulations. Nudging is a widely used technique used to constrain a climate model's large-scale features, aligning them closely with those observed in reanalysis data (*57*, *58*). To mitigate the concern of comparing a nudged simulation directly with the very reanalysis data that served as the source for nudging, we have implemented nudging toward the 6-hourly National Centers for Environmental Prediction (NCEP) reanalysis datasets, with nudging timescale of 6 hours. The primary goal of this experiment is to assess the model's ability to accurately reproduce the interannual variability and long-term trends in AR frequency when the model effectively captures large-scale features, such as the PNA pattern, while retaining the flexibility to simulate other variables and processes.

Various climate modes

The influence of various teleconnection patterns on AR activity has been analyzed over the US west coast to facilitate predictions on different timescales. A variety of climate modes have been considered as main drivers of the changing nature of AR activity, including AO (*39*), Pacific-North America (PNA) teleconnection pattern (*16*, *39*), PJ pattern (*41*), the East Asian subtropical jet (EASJ) (*41*), AMM (*53*), PMM (*59*), PDO (*60*), and ENSO (*4*, *40*). We repeat this correlation analysis to study the relationship between these different climate modes and AR activity over EUS. We also include the NAO in this analysis given its important role in AR activity over the Atlantic sector (*61*). The AO index, NAO index, and PNA index are obtained from the Climate Prediction Center. The AMM index, PMM index, Nino 3.4 index, and PDO index are acquired from the National Oceanic and Atmospheric Administration (NOAA) Physical Sciences Laboratory. The PJ index and EASJ index are calculated following previous studies (*41*). The monthly PNA index from Climate Prediction Center is constructed using the modified pointwise method:

$$\mathrm{PNA} = Z_{\substack{15-25^\circ\mathrm{N}\\180-140^\circ\mathrm{W}}} - Z_{\substack{40-50^\circ\mathrm{N}\\180-140^\circ\mathrm{W}}} + Z_{\substack{45-60^\circ\mathrm{N}\\125-105^\circ\mathrm{W}}} - Z_{\substack{25-35^\circ\mathrm{N}\\90-70^\circ\mathrm{W}}}$$

where Z denotes monthly mean 500-hPa height anomaly calculated with the base period to be 1950–2000. On the basis of the Climate Prediction Center web page, the modified pointwise method–based PNA index is highly correlated with the values from both the rotated empirical orthogonal function (EOF) analysis ($R = 0.92$; $P < 0.01$) and the original pointwise method ($R = 0.98$; $P < 0.01$) (*62*). We use the modified pointwise method to calculate the simulated PNA index but with the base period to be 1980–2000. All the analyses throughout this study cover 1980–2020 winter season (December-January-February) to coincide with MERRA2 datasets. To facilitate mutual comparisons, the ERA5 reanalysis is first interpolated onto the common resolution of 0.5° × 0.625° of MERRA2 and the C192AM4 model.

AR identification algorithm

We use the thresholding IVT global AR detection algorithm documented in (*39*), which uses the high-frequency (6-hourly) zonal and meridional IVT. This approach involves two primary steps.

First, we calculate the IVT threshold to identify potential AR candidates for each grid. This threshold is calculated using an 85th percentile value in this study in combination with a fixed lower limit of 100 kg m^{-1} s^{-1}. To accommodate seasonal variations in IVT, we calculate the 85th percentile for each grid cell over a 5-month period centered on the target month. If the calculated value is smaller than 100 kg m^{-1} s^{-1}, we replace it with this fixed lower limit. This adjustment is essential for regions with consistently low moisture content, such as polar areas, where the 85th percentile of IVT may not effectively identify AR-like structures. The selection of the lower limit is based on manual assessment of its effectiveness in isolating AR-like features in polar regions and aligns with previous AR detection studies in East Antarctica (*4*, *63*). AR candidates are then identified as contiguous regions with IVT values greater than the determined IVT threshold.

Second, these identified "objects" are screened to meet AR criteria, which encompass IVT direction and geometry. The IVT direction criteria include coherence, mean meridional IVT, and consistency with the object's orientation. For coherence, if over half of the grid cells within an AR candidate have IVT directions deviating more than 45° from the object's mean IVT, the object is excluded. This ensures meaningful IVT direction calculations. An object is also excluded if its mean IVT lacks a sufficient poleward component (>50 kg m^{-1} s^{-1}). Additionally, objects are discarded if the mean IVT direction deviates from the object's orientation by more than 45°, removing objects where IVT transport does not align with elongation. Objects retained from the previous step are checked for geometry requirements. We calculate both length and width, discarding AR candidates with a length less than 2000 km or a length-to-width ratio below 2 to match the narrow, elongated features typical of ARs.

Statistical analysis

The grid points within each AR object are used to compute AR frequency and AR-related variables (e.g., IVT and precipitation). AR frequency is defined as the fraction of time a grid cell experiences AR conditions. The associated IVT is used to characterize the AR intensity (*6*). Linear trends of AR frequency and other large-scale circulation fields are calculated based on the Theil-Sen estimator (*64*, *65*), which is robustly insensitive to outliers. The significance level is estimated using the Mann-Kendall test at a significance level of $\alpha = 0.05$. For the correlation analysis, the effective sample size N^* is computed by considering the lag-one autocorrelations of time series following $N^* = N\left(\frac{1-r_1 r_2}{1+r_1 r_2}\right)$, where N is the number of available time steps and r_1 and r_2 are lag-one autocorrelation coefficients of each variable (*66*). We opt not to remove the trend from either the AR frequency or climate modes before conducting the correlation analysis. This decision is supported by the fact that detrending resulted in negligible changes in the results. Additionally, our emphasis in this study is on both the interannual variability and the long-term trend.

Maximum EGR

The maximum EGR is a measure of baroclinic instability, which is extensively used in climate dynamics (*37*, *67*). The EGR is calculated as

$$\mathrm{EGR} = 0.3098 f \left|\frac{\partial U}{\partial z}\right| N^{-1}$$

where f is the Coriolis parameter, U is the zonal wind, z is the vertical height, and N is the Brunt-Väisälä frequency (where $N^2 = \frac{g\partial\theta}{\theta\partial z}$, g being the acceleration due to gravity and θ the potential temperature). EGR is usually calculated at the lower levels of the atmosphere (700 hPa in this study) where major baroclinic development occurs. Following a previous study (*68*), EGR is calculated with daily data and then averaged over seasons.

Composite analysis

To further verify the observed relationship between the PNA pattern with AR activities, mid-latitude jet stream, low-level EGR, and mid-tropospheric geopotential fields, we conduct composite analysis of these fields by constructing their differences between years under strong negative and positive phases of the PNA pattern. In this study, we define years with PNA index values of ±1 as strong positive/negative phases of PNA pattern years, which yields seven samples for the positive PNA composite and six samples for the negative PNA composite.

Statistical prediction model

The effectiveness of the identified relationship between PNA pattern and AR frequency over the EUS is assessed using the leave-one-out cross-validation. We used the leave-one-out cross-validation method in our study. This method is widely used in building statistical prediction models, particularly when dealing with small sample sizes. This method involves the following steps:

1) It starts by temporarily removing one pair of data points (i.e., "leave one out") from the dataset and then uses the remaining data to train the predictive model.

2) The trained model makes predictions for this specific data point, and the mean error for this point is calculated by comparing the model's prediction for the left-out data point with the actual target value.

3) Repeat steps (1) and (2) for every data point. After completing all iterations, the root mean square error, MAE, and correlation coefficient between the predicted and original time series are calculated.

This approach leverages all available data points to construct the predictive model. By consistently using each data point in both training and testing, it minimizes potential biases that might arise from random data subsampling. Here, we use the PNA index as a predictor for AR frequency at both seasonal and monthly scales. Performance metrics, including RMSE, MAE, and correlation coefficient based on the least squares linear regression, are used to assess the accuracy and predictive ability of the model.

Supplementary Materials

This PDF file includes:

Figs. S1 and S15

REFERENCES AND NOTES

1. Y. Zhu, R. E. Newell, A proposed algorithm for moisture fluxes from atmospheric rivers. *Mon. Weather Rev.* **126**, 725–735 (1998).
2. F. M. Ralph, P. J. Neiman, G. A. Wick, Satellite and CALJET aircraft observations of atmospheric rivers over the eastern North Pacific ocean during the winter of 1997/98. *Mon. Weather Rev.* **132**, 1721–1745 (2004).
3. S. H. Baek, J. E. Smerdon, B. I. Cook, A. P. Williams, U.S. Pacific coastal droughts are predominantly driven by internal atmospheric variability. *J. Climate* **34**, 1947–1962 (2021).
4. B. Guan, D. E. Waliser, Detection of atmospheric rivers: Evaluation and application of an algorithm for global studies. *J. Geophys. Res. Atmos.* **120**, 12514–12535 (2015).
5. C. A. Shields, J. J. Rutz, L. R. Leung, F. M. Ralph, M. Wehner, B. Kawzenuk, J. M. Lora, E. McClenny, T. Osborne, A. E. Payne, P. Ullrich, A. Gershunov, N. Goldenson, B. Guan, Y. Qian, A. M. Ramos, C. Sarangi, S. Sellars, I. Gorodetskaya, K. Kashinath, V. Kurlin, K. Mahoney, G. Muszynski, R. Pierce, A. C. Subramanian, R. Tome, D. Waliser, D. Walton, G. Wick, A. Wilson, D. Lavers, A. Collow, H. Krishnan, G. Magnusdottir, P. Nguyen, Atmospheric river tracking method intercomparison project (ARTMIP): Project goals and experimental design. *Geosci. Model Dev.* **11**, 2455–2474 (2018).
6. F. M. Ralph, J. J. Rutz, J. M. Cordeira, M. Dettinger, M. Anderson, D. Reynolds, L. J. Schick, C. Smallcomb, A scale to characterize the strength and impacts of atmospheric rivers. *Bull. Am. Meteorol. Soc.* **100**, 269–289 (2019).
7. Z. Zhang, F. M. Ralph, M. Zheng, The relationship between extratropical cyclone strength and atmospheric river intensity and position. *Geophys. Res. Lett.* **46**, 1814–1823 (2019).
8. F. M. Ralph, T. Coleman, P. Neiman, R. Zamora, M. Dettinger, Observed impacts of duration and seasonality of atmospheric-river landfalls on soil moisture and runoff in coastal northern California. *J. Hydrometeorol.* **14**, 443–459 (2013).
9. M. D. Dettinger, Atmospheric rivers as drought busters on the U.S. west coast. *J. Hydrometeorol.* **14**, 1721–1732 (2013).
10. N. A. Barth, G. Villarini, M. A. Nayak, K. White, Mixed populations and annual flood frequency estimates in the western United States: The role of atmospheric rivers. *Water Resour. Res.* **53**, 257–269 (2017).
11. C. P. Konrad, M. D. Dettinger, Flood runoff in relation to water vapor transport by atmospheric rivers over the western United States, 1949–2015. *Geophys. Res. Lett.* **44**, 11456–11562 (2017).

12. T. W. Corringham, F. M. Ralph, A. Gershunov, D. R. Cayan, C. A. Talbot, Atmospheric rivers drive flood damages in the western United States. *Sci. Adv.* **5**, (2019).
13. B. J. Moore, P. J. Neiman, F. M. Ralph, F. E. Barthold, Physical processes associated with heavy flooding rainfall in Nashville, Tennessee, and vicinity during 1–2 May 2010: The role of an atmospheric river and mesoscale convective systems. *Mon. Weather Rev.* **140**, 358–378 (2012).
14. D. A. Lavers, G. Villarini, Atmospheric rivers and flooding over the central United States. *J. Climate* **26**, 7829–7836 (2013).
15. J. L. Rabinowitz, A. R. Lupo, P. S. Market, P. E. Guinan, An investigation of atmospheric rivers impacting heavy rainfall events in the north-central Mississippi river valley. *Int. J. Climatol.* **39**, 4091–4106 (2019).
16. M. A. Nayak, G. Villarini, A long-term perspective of the hydroclimatological impacts of atmospheric rivers over the central United States. *Water Resour. Res.* **53**, 1144–1166 (2017).
17. E. A. Slinskey, P. C. Loikith, D. E. Waliser, B. Guan, A. Martin, A climatology of atmospheric rivers and associated precipitation for the seven U.S. national climate assessment regions. *J. Hydrometeorol.* **21**, 2439–2456 (2020).
18. D. A. Lavers, G. Villarini, The contribution of atmospheric rivers to precipitation in Europe and the United States. *J. Hydrol.* **522**, 382–390 (2015).
19. N. Debbage, P. Miller, S. Poore, K. Morano, T. Mote, J. A. M. Shepherd, A Climatology of atmospheric river interactions with the southeastern United States coastline. *Int. J. Climatol.* **37**, 4077–4091 (2017).
20. D. K. Miller, C. F. Miniat, R. M. Wooten, A. P. Barros, An expanded investigation of atmospheric rivers in the southern Appalachian Mountains and their connection to landslides. *Atmosphere* **10**, 71 (2019).
21. C. A. Ramseyer, T. J. Stanfield, Z. Van Tol, T. Gingrich, P. Henry, P. Forister, B. Lamkin, S. Stackhouse, S. S. Sauda, Identifying Eastern US atmospheric river types and evaluating historical trends. *J. Geophys. Res. Atmos.* **127**, (2022).
22. M. Teale, D. A. Robinson, Eastern US precipitation investigated through patterns of moisture transport. *Phys. Geogr.* **43**, 589–613 (2022).
23. A. Weisheimer, D. J. Befort, D. MacLeod, T. Palmer, C. O'Reilly, K. Strømmen, Seasonal forecasts of the twentieth century. *Bull. Am. Meteorol. Soc.* **101**, E1413–E1426 (2020).
24. W. Yao, X. Yan, Y. Tang, D. Yang, X. Tan, X. Song, T. Liu, Multidecadal variation in the seasonal predictability of winter PNA and its sources. *Geophys. Res. Lett.* **49**, e2022GL099393 (2022).
25. NOAA National Centers for Environmental Information, Monthly tornadoes report for February 2013; https://www.ncei.noaa.gov/access/monitoring/monthly-report/tornadoes/201302 [accessed 10 November 2022].
26. K. Mahoney, D. L. Jackson, P. Neiman, M. Hughes, L. Darby, G. Wick, A. White, E. Sukovich, R. Cifelli, Understanding the role of atmospheric rivers in heavy precipitation in the southeast United States. *Mon. Weather Rev.* **144**, 1617–1632 (2016).
27. B. Guan, N. P. Molotch, D. E. Waliser, E. J. Fetzer, P. J. Neiman, Extreme snowfall events linked to atmospheric rivers and surface air temperature via satellite measurements. *Geophys. Res. Lett.* **37**, (2010).
28. M. Dettinger, Climate change, atmospheric rivers, and floods in California—A multimodel analysis of storm frequency and magnitude changes. *J. Am. Water Resour. Assoc.* **47**, 514–523 (2011).
29. A. Gershunov, T. Shulgina, F. M. Ralph, D. A. Lavers, J. J. Rutz, Assessing the climate scale variability of atmospheric rivers affecting western North America. *Geophys. Res. Lett.* **44**, 7900–7908 (2017).
30. M. Zhao, Simulations of atmospheric rivers, their variability, and response to global warming using GFDL's new high-resolution general circulation model. *J. Climate* **33**, 10287–10303 (2020).
31. M. Zhao, A study of AR-, TS-, and MCS-associated precipitation and extreme precipitation in present and warmer climates. *J. Climate* **35**, 479–497 (2022).
32. B. Guan, D. E. Waliser, Tracking atmospheric rivers globally: Spatial distributions and temporal evolution of life cycle characteristics. *J. Geophys. Res. Atmos.* **124**, 12523–12552 (2019).
33. C. A. Shields, J. H. Richter, A. Pendergrass, S. Tilmes, Atmospheric rivers impacting western North America in a world with climate *intervention*. *Science* **5**, 41 (2022).
34. F. Bender, V. Ramanathan, G. Tselioudis, Changes in extratropical storm track cloudiness 1983–2008: Observational support for a poleward shift. *Climate Dynam.* **38**, 2037–2053 (2012).
35. M. B. Osman, S. Coats, S. B. Das, J. R. McConnell, N. Chellman, North Atlantic jet stream projections in the context of the past 1,250 years. *Proc. Natl. Acad. Sci. U.S.A.* **118**, e2104105118 (2021).
36. R. Lindzen, B. Farrell, A simple approximate result for the maximum growth rate of baroclinic instabilities. *J. Atmos. Sci.* **37**, 1648–1654 (1980).
37. B. J. Hoskins, P. J. Valdes, On the existence of storm-tracks. *J. Atmos. Sci.* **47**, 1854–1864 (1990).
38. S. Basu, X. Zhang, I. Polyakov, U. S. Bhatt, North American winter-spring storms: Modeling investigation on tropical pacific sea surface temperature impacts. *Geophys. Res. Lett.* **40**, 5228–5233 (2013).
39. B. Guan, N. P. Molotch, D. E. Waliser, E. J. Fetzer, P. J. Neiman, The 2010/2011 snow season in California's Sierra Nevada: Role of atmospheric rivers and modes of large-scale variability. *Water Resour. Res.* **49**, 6731–6743 (2013).
40. A. E. Payne, G. Magnusdottir, Dynamics of landfalling atmospheric rivers over the north pacific in 30 years of MERRA reanalysis. *J. Climate* **27**, 7133–7150 (2014).
41. W. Zhang, G. Villarini, Uncovering the role of the East Asian jet stream and heterogeneities in atmospheric rivers affecting the western united states. *Proc. Natl. Acad. Sci. U.S.A.* **115**, 891–896 (2018).
42. K.-C. Tseng, N. C. Johnson, S. B. Kapnick, T. L. Delworth, F. Lu, W. Cooke, A. T. Wittenberg, A. J. Rosati, L. Zhang, C. McHugh, X. Yang, M. Harrison, F. Zeng, G. Zhang, H. Murakami, M. Bushuk, L. Jia, Are multiseasonal forecasts of atmospheric rivers possible? *Geophys. Res. Lett.* **48**, (2021).
43. J. G. Pinto, M. Reyers, U. Ulbrich, The variable link between PNA and NAO in observations and in multi-century CGCM simulations. *Climate Dynam.* **36**, 337–354 (2011).
44. H. Hersbach, B. Bell, P. Berrisford, S. Hirahara, A. Horányi, J. Muñoz-Sabater, J. Nicolas, C. Peubey, R. Radu, D. Schepers, A. Simmons, C. Soci, S. Abdalla, X. Abellan, G. Balsamo, P. Bechtold, G. Biavati, J. Bidlot, M. Bonavita, G. De Chiara, P. Dahlgren, D. Dee, M. Diamantakis, R. Dragani, J. Flemming, R. Forbes, M. Fuentes, A. Geer, L. Haimberger, S. Healy, R. J. Hogan, E. Hólm, M. Janisková, S. Keeley, P. Laloyaux, P. Lopez, C. Lupu, G. Radnoti, P. de Rosnay, I. Rozum, F. Vamborg, S. Villaume, J.-N. Thépaut, The ERA5 global reanalysis. *Q. J. Roy. Meteorol. Soc.* **146**, 1999–2049 (2020).
45. R. Gelaro, W. McCarty, M. J. Suarez, R. Todling, A. Molod, L. Takacs, C. A. Randles, A. Darmenov, M. G. Bosilovich, R. Reichle, K. Wargan, L. Coy, R. Cullather, C. Draper, S. Akella, V. Buchard, A. Conaty, A. M. da Silva, W. Gu, G. Kim, R. Koster, R. Lucchesi, D. Merkova, J. E. Nielsen, G. Partyka, S. Pawson, W. Putman, M. Rienecker, S. D. Schubert, M. Sienkiewicz, B. Zhao, The modern-era retrospective analysis for research and applications, version 2 (MERRA-2). *J. Climate* **30**, 5419–5454 (2017).
46. J. J. Rutz, C. A. Shields, J. M. Lora, A. E. Payne, B. Guan, P. Ullrich, T. O'Brien, L. R. Leung, F. M. Ralph, M. Wehner, S. Brands, A. Collow, N. Goldenson, I. Gorodetskaya, H. Griffith, K. Kashinath, B. Kawzenuk, H. Krishnan, V. Kurlin, D. Lavers, G. Magnusdottir, K. Mahoney, E. McClenny, G. Muszynski, P. D. Nguyen, M. Prabhat, Y. Qian, A. M. Ramos, C. Sarangi, S. Sellars, T. Shulgina, R. Tome, D. Waliser, D. Walton, G. Wick, A. M. Wilson, M. Viale, The atmospheric river tracking method intercomparison project (ARTMIP): Quantifying uncertainties in atmospheric river climatology. *J. Geophys. Res. Atmos.* **124**, 13777–13802 (2019).
47. B. Guan, D. E. Waliser, N. P. Molotch, E. J. Fetzer, P. J. Neiman, Does the Madden Julian Oscillation influence wintertime atmospheric rivers and snowpack in the Sierra Nevada? *Mon. Weather Rev.* **140**, 325–342 (2012).
48. V. Thandlam, A. Rutgersson, E. Sahlee, Spatio-temporal variability of atmospheric rivers and associated atmospheric parameters in the Euro-Atlantic region. *Theor. Appl. Climatol.* **147**, 13–33 (2022).
49. H. E. Beck, E. F. Wood, M. Pan, C. K. Fisher, D. G. Miralles, A. I. J. M. van Dijk, T. R. McVicar, R. F. Adler, MSWEP v2 global 3-hourly 0.1 precipitation: Methodology and quantitative assessment. *Bull. Am. Meteorol. Soc.* **100**, 473–500 (2019).
50. M. Zhao, J.-C. Golaz, I. M. Held, H. Guo, V. Balaji, R. Benson, J.-H. Chen, X. Chen, L. J. Donner, J. P. Dunne, K. Dunne, J. Durachta, S.-M. Fan, S. M. Freidenreich, S. T. Garner, P. Ginoux, L. M. Harris, L. W. Horowitz, J. P. Krasting, A. R. Langenhorst, Z. Liang, P. Lin, S.-J. Lin, S. L. Malyshev, E. Mason, P. C. D. Milly, Y. Ming, V. Naik, F. Paulot, D. Paynter, P. Phillipps, A. Radhakrishnan, V. Ramaswamy, T. Robinson, D. Schwarzkopf, C. J. Seman, E. Shevliakova, Z. Shen, H. Shin, L. G. Silvers, J. R. Wilson, M. Winton, A. T. Wittenberg, B. Wyman, B. Xiang, The GFDL global atmosphere and land model AM4. 0/LM4. 0: 1. Simulation characteristics with prescribed SSTs. *J. Adv. Model. Earth Syst.* **10**, 691–734 (2018).
51. M. Zhao, J.-C. Golaz, I. M. Held, H. Guo, V. Balaji, R. Benson, J.-H. Chen, X. Chen, L. J. Donner, J. P. Dunne, K. Dunne, J. Durachta, S.-M. Fan, S. M. Freidenreich, S. T. Garner, P. Ginoux, L. M. Harris, L. W. Horowitz, J. P. Krasting, A. R. Langenhorst, Z. Liang, P. Lin, S.-J. Lin, S. L. Malyshev, E. Mason, P. C. D. Milly, Y. Ming, V. Naik, F. Paulot, D. Paynter, P. Phillipps, A. Radhakrishnan, V. Ramaswamy, T. Robinson, D. Schwarzkopf, C. J. Seman, E. Shevliakova, Z. Shen, H. Shin, L. G. Silvers, J. R. Wilson, M. Winton, A. T. Wittenberg, B. Wyman, B. Xiang, The GFDL global atmosphere and land model AM4. 0/LM4. 0: 2. Model description, sensitivity studies, and tuning strategies. *J. Adv. Model. Earth Syst.* **10**, 735–769 (2018).
52. R. J. Haarsma, M. J. Roberts, P. L. Vidale, C. A. Senior, A. Bellucci, Q. Bao, P. Chang, S. Corti, N. S. Fučkar, V. Guemas, J. von Hardenberg, W. Hazeleger, C. Kodama, T. Koenigk, L. R. Leung, J. Lu, J.-J. Luo, J. Mao, M. S. Mizielinski, R. Mizuta, P. Nobre, M. Satoh, E. Scoccimarro, T. Semmler, J. Small, J.-S. von Storch, High resolution model intercomparison project (HighResMIP v1.0) for CMIP6. *Geosci. Model Dev.* **9**, 4185–4208 (2016).
53. T. L. Delworth, W. F. Cooke, A. Adcroft, M. Bushuk, J. H. Chen, K. Dunne, P. Ginoux, R. Gudgel, R. W. Hallberg, L. Harris, M. J. Harrison, N. Johnson, S. B. Kapnick, S. J. Lin, F. Lu, S. Malyshev, P. C. Milly, H. Murakami, V. Naik, S. Pascale, D. Paynter, A. Rosati, M. D. Schwarzkopf, E. Shevliakova, S. Underwood, A. T. Wittenberg, B. Xiang, X. Yang,

F. Zeng, H. Zhang, L. Zhang, M. Zhao, SPEAR: The next generation GFDL modelling system for seasonal to multidecadal prediction and projection. *J. Adv. Model. Earth Syst.* **12**, e2019MS001895 (2020).
54. K. C. Tseng, N. C. Johnson, S. B. Kapnick, W. Cooke, T. L. Delworth, L. Jia, F. Lu, C. McHugh, H. Murakami, A. J. Rosati, A. T. Wittenberg, X. Yang, F. Zeng, L. Zhang, When will humanity notice its influence on atmospheric rivers? *J. Geophys. Res. Atmos.* **127**, (2022).
55. W. Dong, M. Zhao, Y. Ming, V. Ramaswamy, Representation of tropical mesoscale convective systems in a general circulation model: Climatology and response to global warming. *J. Climate* **34**, 5657–5671 (2021).
56. W. Dong, M. Zhao, Y. Ming, J. P. Krasting, V. Ramaswamy, Simulation of United States mesoscale convective systems using GFDL's new high-resolution general circulation model. *J. Climate* **36**, 6967–6990 (2023).
57. J. E. Hoke, R. A. Anthes, The initialization of numerical models by a dynamic-initialization technique. *Mon. Weather Rev.* **104**, 1551–1556 (1976).
58. P. J. Telford, P. Braesicke, O. Morgenstern, J. A. Pyle, Technical Note: Description and assessment of a nudged version of the new dynamics Unified Model. *Atmospheric Chem. Phys.* **8**, 1701–1712 (2008).
59. J. C. Chiang, D. J. Vimont, Analogous Pacific and Atlantic meridional modes of tropical atmosphere–ocean variability. *J. Climate* **17**, 4143–4158 (2004).
60. K. Guirguis, A. Gershunov, T. Shulgina, R. E. Clemesha, F. M. Ralph, Atmospheric rivers impacting Northern California and their modulation by a variable climate. *Climate Dynam.* **52**, 6569–6583 (2019).
61. D. A. Lavers, G. Villarini, The nexus between atmospheric rivers and extreme precipitation across Europe. *Geophys. Res. Lett.* **40**, 3259–3264 (2013).
62. J. M. Wallace, D. S. Gutzler, Teleconnections in the geopotential height field during the Northern Hemisphere winter. *Mon. Weather Rev.* **109**, 784–812 (1981).
63. I. V. Gorodetskaya, M. Tsukernik, K. Claes, M. F. Ralph, W. D. Neff, N. P. Van Lipzig, The role of atmospheric rivers in anomalous snow accumulation in East Antarctica. *Geophys. Res. Lett.* **41**, 6199–6206 (2014).
64. H. Theil, A rank-invariant method of linear and polynomial regression analysis I. *Nederl. Akad. Wetensch. Proc.* **53**, 386–392 (1950).
65. P. Sen, Estimates of the regression coefficient based on Kendall's tau. *J. Am. Stat. Assoc.* **63**, 1379–1389 (1968).
66. C. S. Bretherton, M. Widmann, V. P. Dymnikov, J. M. Wallace, I. Blade, The effective number of spatial degrees of freedom of a time-varying field. *J. Climate* **12**, 1990–2009 (1999).
67. T. M. Merlis, T. Schneider, Scales of linear baroclinic instability and macroturbulence in dry atmospheres. *J. Atmos. Sci.* **66**, 1821–1833 (2009).
68. I. Simmonds, E. P. Lim, Biases in the calculation of Southern Hemisphere mean baroclinic eddy growth rate. *Geophys. Res. Lett.* **36**, (2009).

Acknowledgments: We would like to thank N. C. Johnson and X. Yang for useful discussion and commenting on earlier versions of this paper. **Funding:** This research from the Geophysical Fluid Dynamics Laboratory is supported by NOAA's Science Collaboration Program and administered by UCAR's Cooperative Programs for the Advancement of Earth System Science (CPAESS) under awards NA16NWS4620043 (to W.D.) and NA18NWS4620043B (to W.D.). **Author contributions:** Conceptualization: W.D. Data curation: W.D. Formal analysis: W.D. Funding acquisition: W.D. Investigation: W.D. and M.Z. Methodology: W.D. and M.Z. Project administration: W.D. and M.Z. Resources: W.D. and M.Z. Software: W.D. and M.Z. Supervision: W.D., M.Z., and V.R. Validation: W.D. and V.R. Visualization: W.D. Writing—original draft: W.D. Writing—review and editing: W.D., M.Z., Z.T., and V.R. **Competing interests:** The authors declare that they have no competing interests. **Data and materials availability:** All data needed to evaluate the conclusions in the paper are present in the paper and/or the Supplementary Materials. The Multi-Source Weighted-Ensemble Precipitation, version 2 (MSWEP V2) precipitation data can be found at https://gloh2o.org/mswep/. The monthly AMM index, PMM index, Nino 3.4 index, and PDO index can be found at NOAA Physical Sciences Laboratory website (https://psl.noaa.gov/data/timeseries/monthly/). The monthly PNA index is downloaded from the Climate Prediction Center (https://www.cpc.ncep.noaa.gov/products/precip/CWlink/pna/pna.shtml). The ERA5 and MERRA2 reanalysis datasets can be found at https://apps.ecmwf.int/data-catalogues/era5/ and https://gmao.gsfc.nasa.gov/reanalysis/MERRA-2/, respectively. The C192AM4 model outputs can be downloaded from https://esgf-node.llnl.gov/search/cmip6/. The GFDL AM4 model source code can be obtained from https://data1.gfdl.noaa.gov/nomads/forms/am4.0/. All custom codes are direct implementation of standard methods and techniques, described in detail in Materials and Methods.

Submitted 20 June 2023
Accepted 22 December 2023
Published 24 January 2024
10.1126/sciadv.adj3325